




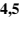

Geochemistry, Geophysics, Geosystems®



RESEARCH ARTICLE

10.1029/2022GC010752

Rupture Geometry and Slip Distribution of the Mw 7.2 Nippes Earthquake, Haiti, From Space Geodetic Data

B. Raimbault¹ , R. Jolivet^{1,2} , E. Calais^{1,2,3,4} , S. Symithe^{4,5} , Y. Fukushima⁶ , and P. Dubernet¹

Key Points:

- We present geodetic observations (Global Navigation Satellite System and Interferometric Synthetic Aperture Radar) constraining the slip distribution of the Haiti Nippes earthquake, 2021, on two faults
- Mechanisms of the 2010 and 2021 earthquakes confirm the interseismic accumulation of transpressional strain within the Southern Peninsula
- We highlight the role of segmentation on dynamics of stress release along the Enriquillo-Plantain Garden Fault system with significant implications on seismic hazard

Supporting Information:

Supporting Information may be found in the online version of this article.

Correspondence to:

B. Raimbault,
bryan.raimbault@normalesup.org

Citation:

Raimbault, B., Jolivet, R., Calais, E., Symithe, S., Fukushima, Y., & Dubernet, P. (2023). Rupture geometry and slip distribution of the Mw 7.2 Nippes earthquake, Haiti, from space geodetic data. *Geochemistry, Geophysics, Geosystems*, 24, e2022GC010752. <https://doi.org/10.1029/2022GC010752>

Received 20 OCT 2022

Accepted 7 FEB 2023

Author Contributions:

Conceptualization: B. Raimbault, R.

Jolivet, E. Calais

Formal analysis: B. Raimbault, R.

Jolivet, E. Calais

Funding acquisition: R. Jolivet, E.

Calais, S. Symithe

Investigation: B. Raimbault, S. Symithe,

Y. Fukushima

¹Laboratoire de Géologie, Département de Géosciences, École normale supérieure, CNRS, UMR 8538, PSL University, Paris, France, ²Institut Universitaire de France, Paris, France, ³Observatoire de la Côte d'Azur, Géoazur, Institut de Recherche pour le Développement, CNRS, Université Côte d'Azur, Valbonne, France, ⁴CARIBACT Joint Research Laboratory, Institut de Recherche pour le Développement, Université d'État d'Haïti, Université Côte d'Azur, Port-au-Prince, Haïti, ⁵Faculté des Sciences, URGéo, Université d'État d'Haïti, Port-au-Prince, Haïti, ⁶International Research Institute of Disaster Science, Tohoku University, Sendai, Japan

Abstract On 14 August 2021 the Mw 7.2 Nippes earthquake struck southern Haiti, rupturing a segment of the Enriquillo-Plantain Garden Fault system (EPGF), a 300 km-long strike-slip fault system that accommodates half of the highly oblique convergence displacement between the Caribbean and the North American plates. We use coseismic surface displacements from Interferometric Synthetic Aperture Radar and Global Navigation Satellite System (GNSS) to estimate the geometry of the rupture through a systematic parametric exploration, determine its mechanism, and relate them to the regional tectonics derived from interseismic GNSS measurements. We show that the earthquake ruptured a north dipping fault ($66 \pm 4^\circ$ dip) with a geodetically determined moment release that is 40% reverse and 60% strike-slip. We cannot conclude whether this north-dipping structure is the EPGF itself or a distinct fault running parallel to the EPGF. The rupture then evolved to the west on a vertical ($86 \pm 2^\circ$ dip) fault parallel to the EPGF, the Ravine du Sud fault, with left-lateral strike-slip motion. The coseismic slip distribution of the 2010 Léogane and 2021 Nippes earthquakes, consistent with the transpressional interseismic strain rate field, show a segmentation of the Caribbean–North American plate boundary in southern Haiti and imply a revision in our understanding of the mode of earthquake rupture within the EPGF system.

Plain Language Summary On 14 August 2021, a magnitude Mw 7.2 earthquake struck the Southern Peninsula of Haiti, a Caribbean country highly vulnerable to natural hazards. Haiti's Peninsula is the locus of the Enriquillo-Plantain Garden Fault (EPGF), known to accumulate elastic strain susceptible to be released in earthquakes to come. We use satellite radar images and Global Navigation Satellite System (GNSS) data acquired in the epicentral areas of the earthquake to investigate the geometry of the fault involved in the earthquake, the fault motion, and how they match the long-term, decadal-scale, regional deformation pattern derived from GNSS data. We show that the earthquake first ruptured a north-dipping fault ($66 \pm 4^\circ$) and continued to the west on a vertical strike-slip ($86 \pm 2^\circ$) fault corresponding to the mapped Ravine du Sud fault. We cannot conclude whether this north-dipping structure is the EPGF itself or a distinct fault running parallel to the EPGF. We show that the fault motion during the earthquake is consistent with the long-term deformation pattern, with strong similarities with the devastating 2010 event which did not rupture the EPGF. These events show an unexpected segmentation of the fault system that is not yet accounted for in the regional earthquake hazard maps.

1. Introduction

On 14 August 2021, a Mw 7.2 earthquake struck the Southern Peninsula of Haiti causing 2,248 deaths, with more than 12,760 people injured, and damaging or destroying at least 137,500 buildings (PDNA, 2021). The epicenter is located in the Nippes province (Calais, Symithe, Monfret, et al., 2022; Okuwaki & Fan, 2022), ~100 km west of the Léogâne fault that ruptured in the Mw 7.0 earthquake of 12 January 2010 (Calais et al., 2010; Douilly et al., 2013; Hayes et al., 2010). These two events mark a renewal of activity after more than two centuries of seismic quiescence since the series of large and destructive earthquakes that struck southern Haiti in 1701, 1751, and 1770 (Figure 1a) (Bakun et al., 2012; Scherer, 1912). These large historical earthquakes in southern Haiti are often interpreted as strain release on the Enriquillo-Plantain Garden Fault (EPGF), the EW-trending left-lateral strike-slip fault that marks the boundary between the Caribbean and Gonave plates (Figure 1a). Global

© 2023. The Authors.

This is an open access article under the terms of the [Creative Commons Attribution-NonCommercial-NoDerivs License](https://creativecommons.org/licenses/by-nc-nd/4.0/), which permits use and distribution in any medium, provided the original work is properly cited, the use is non-commercial and no modifications or adaptations are made.

Methodology: B. Raimbault, R. Jolivet, E. Calais

Project Administration: R. Jolivet, E. Calais, P. Dubernet

Resources: S. Symithe, Y. Fukushima, P. Dubernet

Software: P. Dubernet

Supervision: R. Jolivet, E. Calais

Validation: B. Raimbault

Visualization: B. Raimbault

Writing – original draft: B. Raimbault

Writing – review & editing: R. Jolivet, E. Calais, S. Symithe, Y. Fukushima

Navigation Satellite System (GNSS) geodetic measurements combined with kinematic block models indicate 7 ± 2 mm/yr of slip on the EPGF, while the remainder of the ~ 19 mm/yr of highly oblique convergence between the Caribbean and North American plates (DeMets et al., 2000) is distributed on the Septentrional strike-slip fault and the North Hispaniola thrust fault offshore to the north of the island (Benford et al., 2012; Manaker et al., 2008; Symithe et al., 2015).

A number of recent observations indicate that southern Haiti is also the locus of a significant but overlooked component of shortening perpendicular to the direction of the mostly strike-slip plate boundary. For instance, a third of the seismic moment of the 12 January 2010, Mw 7.0 earthquake was released on a north-dipping fault sub-parallel to the major EPGF left-lateral strike-slip fault (Calais et al., 2010; Hayes et al., 2010). Interseismic GNSS measurements in southeastern Haiti document an active fault dipping to the south underneath the Massif de la Selle that accommodates 9 mm/yr of reverse and 6 mm/yr of left-lateral strike-slip motion (Symithe & Calais, 2016). This kinematics is consistent with the geological mapping of compressional structures along the southern edge of the Cul-de-Sac plain (Saint Fleur et al., 2019) and with the seismic imaging of a south-dipping reverse fault under the Massif de La Selle–Bahoruco (Possee et al., 2019; Rodriguez et al., 2018). However, the spatial and temporal distribution of this interseismic transpressional strain is still poorly documented. In particular, it is unclear which faults might release this combined strike-slip/compressional strain and whether strike-slip and thrust earthquakes are decoupled onto different structures. This has a direct bearing on regional seismic hazard estimations, as current maps only consider strike-slip sources (Frankel et al., 2011).

The 14 August, Mw 7.2 Nippes earthquake is the most recent example of this dual mode of strain release in southern Haiti. Okuwaki and Fan (2022) and Calais, Symithe, Monfret, et al. (2022) used multiple geophysical data sets to show that the rupture likely initiated on a reverse thrust fault segment, then transitioned westward to a steeper, strike-slip, fault segment. Maurer et al. (2022) reached a similar conclusion, though using a more complex rupture geometry, including 5 fault segments inferred from geological mapping. The 2010 and 2021 earthquakes therefore appear to bear similarities in that they ruptured limited portions of the EPGF system with a combination of thrust and strike-slip on multiple segments. The question whether the 2021 earthquake ruptured the EPGF itself or secondary structures part of the EPGF system remains open.

Here, we jointly use surface displacements from Interferometric Synthetic Aperture Radar (InSAR) together with 3-dimensional, near-field GNSS measurements of coseismic displacements to constrain the spatial extent, geometry, and slip distribution of the earthquake rupture. We find that the two geodetic data sets are well-fitted by the dual rupture of (a) a north-dipping segment with a geodetically determined moment release that is 40% reverse and 60% strike-slip, and (b) a sub-vertical fault parallel to the EPGF, the Ravine du Sud fault, with almost purely left-lateral strike-slip motion. Using an improved interseismic GNSS velocity field, we then show that transpression across the Caribbean–North America plate boundary focuses in the Southern Peninsula of Haiti, consistent with the strain released during the 2010 and 2021 earthquakes.

2. Geodetic Observations

2.1. InSAR and GNSS Coseismic Displacements

2.1.1. InSAR Data and Processing

We use Sentinel 1-A and 1-B and ALOS-2 radar images acquired before and after the 2021 Nippes earthquake to derive the coseismic surface displacement field. We compute coseismic interferograms shown in Figure 2b from Sentinel 1 acquisitions descending track 142 on 3 and 15 August 2021. We use ALOS-2 Stripmap acquisitions along an ascending track on 23 December 2020 and 18 August 2021 and wide-swath acquisitions along a descending track on 10 December 2019 and 17 August 2021.

Sentinel radar images were acquired in TOPS mode (Terrain Observation by Progressive Scan), resulting in 250 km wide swath tiles of Single Look Complex images which we processed with the ISCE processing chain (Rosen et al., 2012, JPL/CalTech). SAR images are coregistered using restituted orbital information provided by the European Space Agency. Coregistration is refined using the spectral diversity approach (Fattahi et al., 2016) on burst overlap regions. Topography contribution is removed using the digital elevation model from the Shuttle Radar Topography Mission (SRTM, Farr et al., 2007). Differential interferograms between pairs of images are computed burst by burst and stitched together into a single image. We downsample the raw interferogram

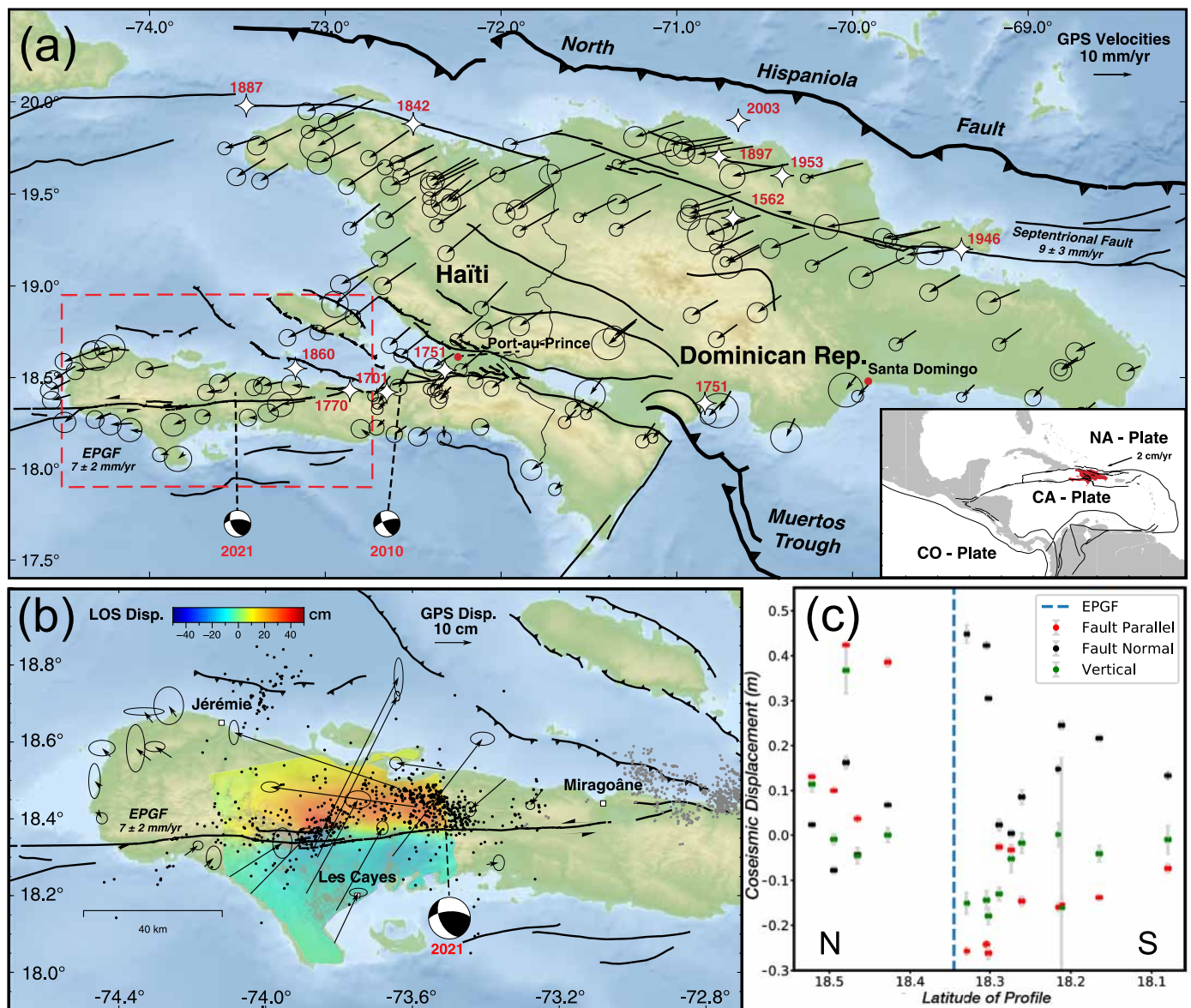


Figure 1. (a) Seismotectonic setting of Hispaniola Island. Regional map (bottom right inset) shows the current motion of the North-American plate (NA-Plate) with respect to the Caribbean plate (CA-Plate). Black lines are fault traces from Saint Fleur et al. (2020). Black arrows in panel (a) are Global Navigation Satellite System (GNSS)-derived interseismic velocities with respect to the Caribbean plate from continuous and campaign acquisitions. Error ellipses are 95% confidence interval. White stars indicate major historical earthquakes (Bakun et al., 2012; Scherer, 1912). Focal mechanisms are from USGS for the Léogâne (12 January 2010) and Nippes (14 August 2021) earthquakes (USGS, 2021). Red dashed rectangle in panel (a) shows the footprint of panel (b). (b) Seismotectonic context of the 2021 Nippes earthquake. Gray dots are relocated aftershocks of the 2010 earthquake from Douilly et al. (2016), black dots are relocated aftershocks from Calais, Symithe, Monfret, et al. (2022) derived from the Ayiti-Séismes platform. Black arrows show the GNSS-derived coseismic displacement associated with the 14 August, Mw 7.2 Nippes earthquake. Error ellipses are 95% confidence interval. ALOS-2 SAR ascending interferogram showing LOS deformation of the Nippes earthquake is overlaid. (c) Coseismic displacements along a north-south profile (~90 km long and ~100 km wide) across southern Haiti at 73.7°W longitude. Coseismic displacement is projected onto directions normal and parallel to the Enriquillo-Plantain Garden Fault. Uncertainties associated with each displacement value are shown in gray. EPGF, Enriquillo-Plantain Garden Fault.

(“multilooking”) to improve coherence. We apply 12 looks in azimuth and 48 looks in range directions for a final pixel size of 170 × 110 m. We model and correct atmospheric phase delays due to spatio-temporal variations of tropospheric conditions using the ECMWF-ERA5 global reanalysis of atmospheric data (PyAPS package, Jolivet et al., 2011, 2014a). We filter the interferogram using a phase adaptive filter (Goldstein & Werner, 1998) and unwrap it using SNAPHU, a statistical minimum cost-flow approach (Chen & Zebker, 2002). We mask Sentinel interferogram pixels with a coherence lower than 0.35. We exclude from the analysis the Sentinel-1

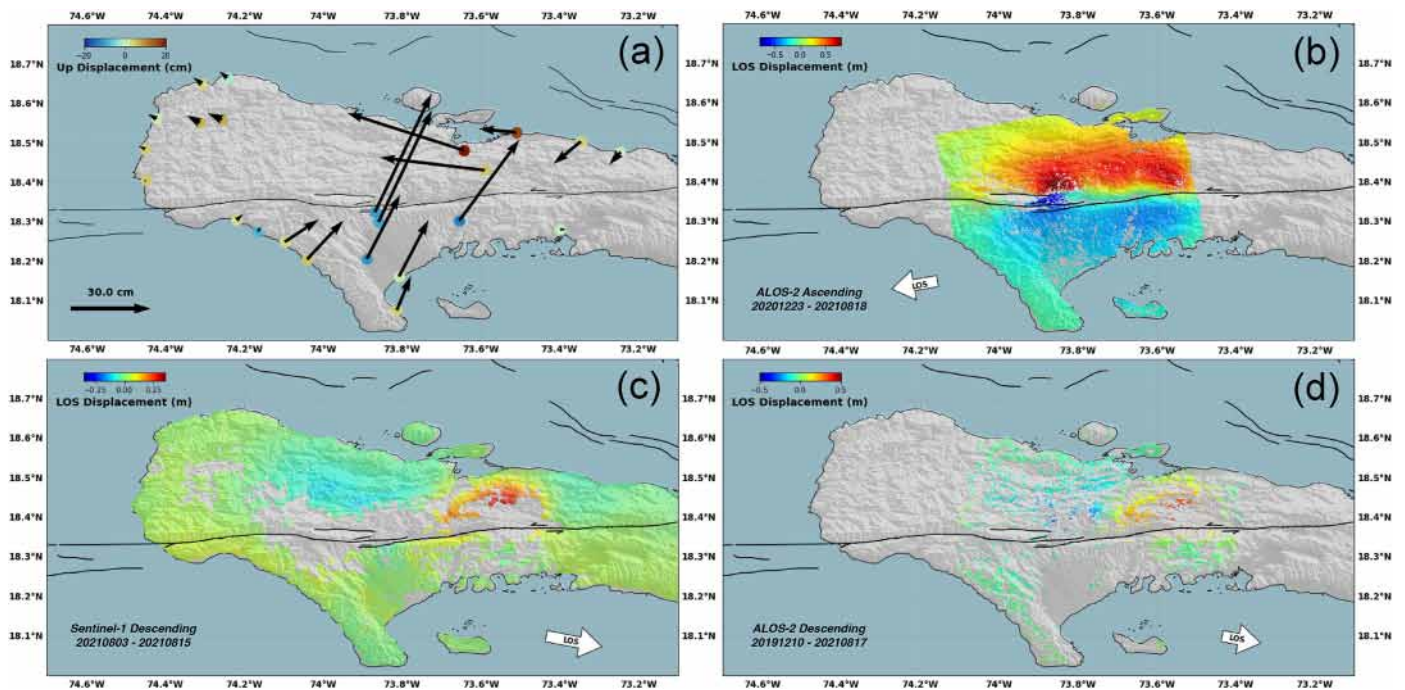


Figure 2. Geodetic Datasets—Global Navigation Satellite System (GNSS) coseismic displacements and unwrapped coseismic interferograms of the Mw 7.2 Nippes earthquake used in this study. White arrows represent the surface projection of the LOS vector from the ground toward the satellite. (a) GNSS-derived coseismic displacements associated resulting from the 14 August, Mw 7.2 Nippes earthquake. Colored dots are the GNSS-derived coseismic vertical displacement. The displacement at site BARZ (~ 0.36 m) is saturated to highlight variations of vertical displacements at other stations. (b) Surface displacement in the satellite line-of-sight (LOS) direction from the Sentinel-1 (S1) descending interferogram formed from acquisitions on track 142 on 3 and 15 August 2021. (c) ALOS-2 ascending interferogram formed from acquisitions on track 43 on 23 December 2020 and 18 August 2021. (d) ALOS-2 descending interferogram formed from acquisitions on track 138 on 10 December 2019 and 17 August 2021.

ascending coseismic interferograms due to very low coherence resulting in unwrapping errors close to the EPGF (see Figures S5–S7 and S18–S21 in Supporting Information S1 for a comparative analysis in which we use Sentinel-1 ascending interferograms).

ALOS-2 radar images are acquired in Stripmap (SM) and ScanSAR (WD) modes resulting in swaths of 70 and 350 km width, respectively, which we processed using the RINC processing chain (Ozawa et al., 2016). We coregister ALOS-2 SAR images and remove the topographic contribution using the digital ellipsoidal height models created from the hole-filled SRTM digital elevation models (Jarvis et al., 2008) and the EGM96 geoid model (Lemoine et al., 1997). Differential interferograms are computed using the coregistered SLCs and down-sampled with a spatial averaging (“multilooking”) before unwrapping them. We multilook in the range and azimuth directions by 8 and 15 for the Stripmap images and by 8 and 36 for the ScanSAR images. We filter the images (Baran et al., 2003) and unwrap them using SNAPHU (Chen & Zebker, 2002). Final pixel size is approximately 50×50 m and 110×110 m for the stripmap and wideswath interferograms, respectively. We finally mask pixels with a coherence lower than 0.05 for the Stripmap interferogram and 0.13 for the ScanSAR one to keep the surface rupture features.

2.1.2. GNSS Data and Processing

The 150 velocities used here are a subset of a ~ 500 -station data set covering the whole Caribbean region that we process on a routine basis. It includes mostly continuously operating stations except for Haiti, where the data come primarily from repeated campaign measurements.

We use the GAMIT-GLOBK software package (Herring et al., 2010) to process the double-difference GNSS phase measurements using the International GNSS Service (IGS) and Earth orientation parameters from the International Earth Rotation Service to produce loosely constrained daily solutions. We then combine these regional solutions with global daily solutions for the whole IGS network available from the Massachusetts Institute of Technology IGS Data Analysis Center. These solutions are finally combined into a single position/velocity

solution, which we tie to the International Terrestrial Reference Frame (ITRF2014, Altamimi et al., 2016) by minimizing position and velocity deviations from a set of globally defined IGS reference sites common to our solution via a 12-parameter Helmert transform. We then rotate the velocities into a Caribbean-fixed reference frame using a Caribbean-wide kinematic block model (Meade & Loveless, 2009), following the same procedure as described in detail in Symithe et al. (2015), resulting in the interseismic velocity field displayed in Figure 1a.

We obtain the coseismic displacement at GNSS sites by estimating an offset at the date of the earthquake (see Table S1 in Supporting Information S1). At continuous stations, we directly determine the offset using 1 week of pre- and post-earthquake data. This only concerns 4 sites in southern Haiti (ANSV, CAMY, JACX, JME2, see Figure S1 in Supporting Information S1). At campaign sites, we fit the entire position time series available and impose the interseismic velocity determined using the pre-earthquake data set while solving for an offset at the date of the earthquake. We only use sites with at least 3 pre-earthquake measurement epochs over a time interval of at least 5 years, with well-determined interseismic velocities. Post-earthquake data were acquired between 17 and 31 August 2021, with three to five 24-hr-long measurement sessions at each site.

2.1.3. Coseismic Ground Displacement

The interferograms shown in Figure 2 provide a complete coverage of the earthquake rupture from three different viewing geometries. The ALOS-2 ascending interferogram shows motion toward the satellite from the epicentral region in the western part of the rupture area (74° and 73.5°W), whereas both descending interferograms show motion toward the satellite only in the epicentral area and away from the satellite from 73.7°W to the westernmost part of the rupture ($\sim 74^\circ\text{W}$). Motion toward the satellite in the epicentral area in both geometries indicate that LOS motion is dominated by uplift, with up to ~ 50 cm of displacement in the LOS direction. The opposite sense of motion on ascending and descending interferograms in the western part of the rupture indicates that motion is mostly horizontal and left-lateral. Moreover, the sharp color gradient on the ALOS-2 stripmap interferogram near $18.38^\circ\text{N}/73.9^\circ\text{W}$ on Figure 2b suggests that the rupture reached the surface in its western part, coincident with the left-lateral strike-slip Ravine du Sud fault mapped by Saint Fleur et al. (2020).

GNSS-derived coseismic displacement shown in Figures 1b and 2a are consistent with motion derived from the interferograms. GNSS stations located north of the EPGF show westward motion from the epicentral area, whereas those located south of the EPGF show mostly northward displacements. Combined horizontal and vertical displacement reach 0.63 m at station BARZ ($73.64^\circ\text{W}/18.48^\circ\text{N}$), the closest to the epicenter. A north-south profile perpendicular to the EPGF of the coseismic displacements (Figure 1c) confirms that the earthquake released both left-lateral strike-slip motion parallel to the EPGF and north-south shortening normal to the EPGF. GNSS-derived coseismic displacement shows up to ~ 0.4 m of shortening, up to ~ 0.55 m of left-lateral motion, and up to ~ 0.2 m of vertical motion. Since the post-earthquake GNSS field survey took place during the 2 weeks following the event, it may include a contribution of early postseismic displacements. Radar interferograms indeed show cm-level afterslip during the first few days after the event (Figure S17 in Supporting Information S1, Maurer et al., 2022; Yin et al., 2022). Since afterslip appears to be restricted to the first kilometers of the crust at depth, we only expect a sub-centimeter contribution at the GNSS sites in that area, although deeper post-seismic processes cannot be excluded.

Coseismic ground displacement therefore show that the Nippes earthquake combined left-lateral strike-slip motion with a significant component of north-south shortening, as observed during the 2010, Mw 7.0 event along the fault system ~ 100 km to the east (Figure 1b). Such oblique motion is consistent with the current transpressional tectonic regime in southern Haiti, where long-term interseismic deformation appears to be partitioned between left-lateral strike-slip motion on the EPGF and a plate boundary-perpendicular shortening further north (Calais et al., 2010, 2016). In the following, we use the coseismic ground displacement derived from InSAR and GNSS to determine the geometry of the rupture and the coseismic slip distribution that best fits both data sets.

3. Coseismic Slip Inversion and Geometry Exploration

3.1. Fault Geometry Exploration

Several studies have already proposed finite fault solutions for the 2021 Nippes earthquake rupture. The U.S. Geological Survey (USGS, 2021) used long-wavelength teleseismic data and far-field GNSS data to propose the rupture of a single north-dipping fault, which surface trace coincides with the EPGF. In their model, the

earthquake initially ruptured an oblique-slip segment with 50% strike-slip and dip-slip motion, then propagated westward with mostly left-lateral strike-slip. Okuwaki and Fan (2022) used teleseismic data to propose that the earthquake (a) ruptured two fault segments that do not align with the EPGF, (b) initiated with a significant reverse component, and (c) jumped westward to a segment oriented 45° from the direction of the EPGF. That last assertion does not match InSAR data (see above) or aftershock relocations (Douilly et al., 2022). Calais, Symithe, Monfret, et al. (2022), in a study that emphasized the role of citizen-hosted seismometers in a development context, combined precise aftershock relocations with seismic and InSAR data to propose the rupture of two north-dipping fault segments. In their model, the first segment to the east, with a ~60° dip and a ~263° azimuth, involved mostly dip-slip reverse motion, with a surface projection compatible with the mapped trace of the EPGF. They propose that the rupture propagated westward on a steeply dipping fault segment coinciding with the Ravine du Sud fault, with mostly strike-slip motion. Maurer et al. (2022) used InSAR data similar to the ones used here to infer that the earthquake involved a complex rupture of 5 segments within the EPGF system. Here we improve over the limitations of previous studies by using all the geodetic data currently available, including near-field coseismic GNSS horizontal and vertical data (Figure 2), and by systematically exploring the simplest possible geometry of the rupture.

We build a generic fault geometry starting from the non-linear inversion model described in Calais, Symithe, Monfret, et al. (2022), which we extend laterally using the surface fault traces of the RSF, EPGF, and geologically mapped fault traces from Saint Fleur et al. (2020) to account for possible coseismic slip to the east and west of those segments. We mesh our generic geometry with triangular elements (Figures S8 and S9 in Supporting Information S1) using the python implementation of “distmesh” (Persson & Strang, 2004). Triangular patches have a 2 km length at the surface and their along-dip size increases with depth by a tenth of their depth. Starting with the generic geometry described above, we generate all the other dip combinations by rotating faults around the axis line between fault traces terminations. For each fault dip angle, that is, from 0° to 90°, we compute the Green's functions assuming a stratified elastic half space (Zhu & Rivera, 2002) using profiles of P- and S-wave velocity (see Figure S10 in Supporting Information S1) from a previous seismological study of the region by Douilly et al. (2016). Our elastic structure may not align with the findings of most recent studies (Douilly et al., 2022) and might result in a slight overestimation of the derived seismic moments. Then, we explore the dip angles from 0° to 90° for the modeled RSF and north-dipping thrust to determine the coseismic slip distribution that minimizes the misfit between model prediction and geodetic data, that is, GNSS and atmospheric-corrected InSAR. All computations are done using the CSI package (Elliott et al., 2016; Jolivet et al., 2015, <https://github.com/jolivet/csi>).

3.2. Coseismic Slip Inversion

Assuming a vector \mathbf{m} of slip values on a fault, together with Green's functions relating fault unit slip to surface displacement \mathbf{G} , one can compute a prediction of surface displacements \mathbf{d} as $\mathbf{d} = \mathbf{G}\mathbf{m}$. The inversion strategy here is to find, by exploring all combinations of dip angles for both faults, the vector \mathbf{m} of slip values that is consistent with the geodetic data \mathbf{d}_{obs} . We downsample the three coseismic interferograms using a quadtree approach (Welstead, 1999) guided by the distance to the EPGF trace (Jolivet et al., 2014b, 2015; Saint Fleur et al., 2020) and use the 3D GNSS coseismic displacements (see Figure S11 in Supporting Information S1 and Figure 2a). We use the SLSQP method of Scipy (Virtanen et al., 2020) to minimize the least-square function defined as (e.g., Tarantola, 2005):

$$S(\mathbf{m}) = (\mathbf{G}\mathbf{m} - \mathbf{d}_{obs})^T \mathbf{C}_d^{-1} (\mathbf{G}\mathbf{m} - \mathbf{d}_{obs}) + (\mathbf{m}_p - \mathbf{m})^T \mathbf{C}_m^{-1} (\mathbf{m}_p - \mathbf{m}) \quad (1)$$

where \mathbf{C}_d is the data covariance matrix of each downsampled interferogram and \mathbf{m}_p the prior model (here, the null vector), \mathbf{C}_m is the model covariance matrix described in Radiguet et al. (2010) as

$$\mathbf{C}_m(i, j) = \left(\sigma \frac{\lambda_0}{\lambda} \right)^2 \exp\left(\frac{-d(i, j)}{\lambda} \right) \quad (2)$$

where $d(i, j)$ is the distance between nodes, λ_0 is a normalizing distance, λ is a correlation length along horizontal and along-dip directions, and σ is the a priori standard deviation of the model parameters fixing the amplitude of the correlation. \mathbf{C}_m is a regularization scheme similar to a spatial smoothing that penalizes unrealistic slip distribution. Slip on the fault is defined as the linear interpolation between slip values at each vertex of the triangular mesh. We test several horizontal and vertical length-scale values to find values of λ and σ that

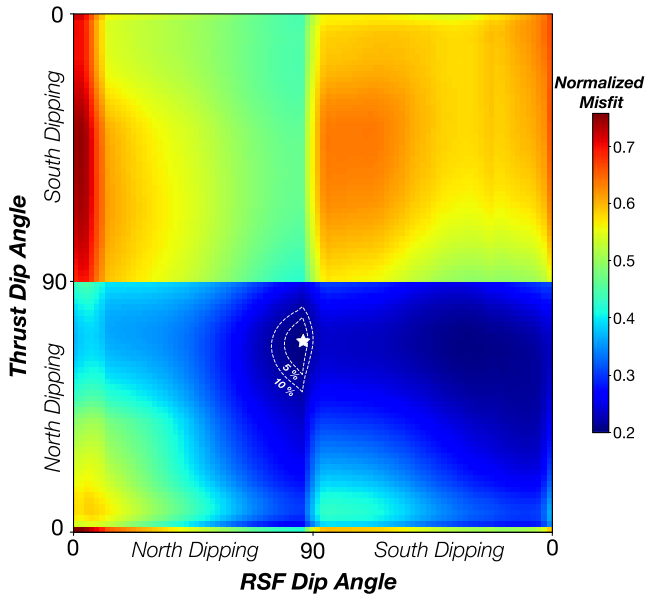


Figure 3. Normalized misfit from the systematic exploration of all possible dip angle combinations for the Ravine du Sud Fault (RSF) and the north-dipping thrust. The white star shows the combination of dip angles that minimizes the model misfit to the Interferometric Synthetic Aperture Radar and Global Navigation Satellite System data. The best geometrical combinations is for a dip angle of 66° north for the thrust segment, and 86° for the RSF, with a normalized misfit value of 19%. White dashed lines indicate the 5% and 10% deviation from the optimal combination.

optimizes data misfit to model roughness. In the end, we use the values of $\lambda = 1$ km, $\lambda_0 = 0.2$ km (minimal distance between nodes) and $\sigma = 2$ m. In the inversion, we account for additional long-wavelength artifacts and possible orbital errors on InSAR data with a second-order polynomial function. For each couple of dip angles for the modeled RSF and thrust segment, we solve for strike-slip and dip-slip motion on each fault and calculate the associated normalized misfit between model prediction and geodetic data as:

$$\Theta = (\mathbf{Gm} - \mathbf{d}_{obs})^T \mathbf{C}_d^{-1} (\mathbf{Gm} - \mathbf{d}_{obs}) / (\mathbf{d}_{obs}^T \mathbf{C}_d^{-1} \mathbf{d}_{obs}) \quad (3)$$

with \mathbf{Gm} the data prediction, \mathbf{d}_{obs} the coseismic (InSAR + GNSS) data and \mathbf{C}_d the data covariance matrix derive from the covariance function of interferograms describing the noise of the measurement (Jolivet et al., 2012; Sudhaus & Jónsson, 2009). Θ estimates the proportions of the norm of the residues that corresponds to the norm of the data.

Results from all tested geometrical configurations (Figure 3) show that the data effectively favor a north-dipping thrust, while the dip of the RSF segment is less well-determined. This wider range of possible dip angles for the RSF segment reflects the fact that slip on the RSF is mostly horizontal (i.e., strike-slip), as shown by the geodetic observations and other studies (Calais, Symithe, Monfret, et al., 2022; Maurer et al., 2022; Okuwaki & Fan, 2022; USGS, 2021). We choose to discard all the south-dipping options for the RSF segment as this kind of structure is quite unlikely in mainly strike-slip contexts. Besides, as we are uncertain if the north-dipping structure we modeled is the EPGF or a separate thrust running parallel to the EPGF, we refer to it as the north-dipping thrust. We find that the misfit is lowest for a RSF segment dipping to the north at a $86 \pm 2^\circ$ angle (within 5% error) and a thrust segment dipping to the north at a $66 \pm 4^\circ$ angle (within 5% error). The

hypocenter location from Calais, Symithe, Monfret, et al. (2022) matches that latter rupture segment at depth. The square-root of the variance of residuals displacements (RMSE), a measure of the model misfit, ranges between 0.01 m misfit for the Sentinel descending track, 0.09 m for the ALOS-2 SM acquisition, 0.05 m for the ALOS-2 WD acquisition, and 0.08 m for the GNSS data (Figure 4). The model shows similar or even better residuals compared to the study of Maurer et al. (2022) without the uses of low coherence areas in interferograms of low quality. Our model slightly underestimates surface displacements visible in the ALOS-2 stripmap data only near the fault surface rupture, around $73.9^\circ\text{W}/18.35^\circ\text{N}$, an area that is masked in other viewing geometries which might also holds early postseismic deformation. We therefore conclude that this two-segment rupture geometry is sufficient to explain the bulk of the InSAR and GNSS observations.

The preferred coseismic model, which 3D geometry is shown in Figure 5a, is characterized by a combination of reverse and strike-slip motion at depth between 10 and 20 km on the north-dipping thrust and left-lateral strike-slip at shallow depth (<7 km) on the RSF segment. The model shows a maximum coseismic slip of 2.95 m at a depth of 12 km on the north-dipping thrust and 2.61 m at a depth of 4 km on the RSF. Dip-slip distribution (Figure S13 in Supporting Information S1) along the north-dipping thrust shows a large area of reverse motion which connects with the RSF to the west. Large slip along the RSF is shallow (<7 km wide) and does not extend below the intersection between the north-dipping thrust and RSF segments. The distribution of strike-slip motion shows a similar pattern (Figure S14 in Supporting Information S1), with the addition of a second patch of slip of lower amplitude (~ 150 cm) on the north-dipping thrust toward the RSF main slipping patch.

The model that best-fits both GNSS and InSAR data shows that the north-dipping thrust and RSF segments released an amount of slip equivalent to a moment magnitude of Mw 7.19 and Mw 6.83, respectively. The overall slip distribution estimated here corresponds to a total seismic moment of 1×10^{20} N-m, equivalent to a moment magnitude of Mw 7.2, in agreement with seismological estimates (Calais, Symithe, Monfret, et al., 2022; Okuwaki & Fan, 2022; USGS, 2021). The earthquake released strike-slip and dip-slip seismic moments of 8.4×10^{19} N-m and 5.2×10^{19} N-m, respectively, with 4.3×10^{19} N-m (40%) of reverse and 6.4×10^{19} N-m (60%) of strike-slip moment on the north-dipping thrust, and 9.7×10^{18} N-m (30%) of reverse and 2.1×10^{19} N-m (70%) of strike-slip

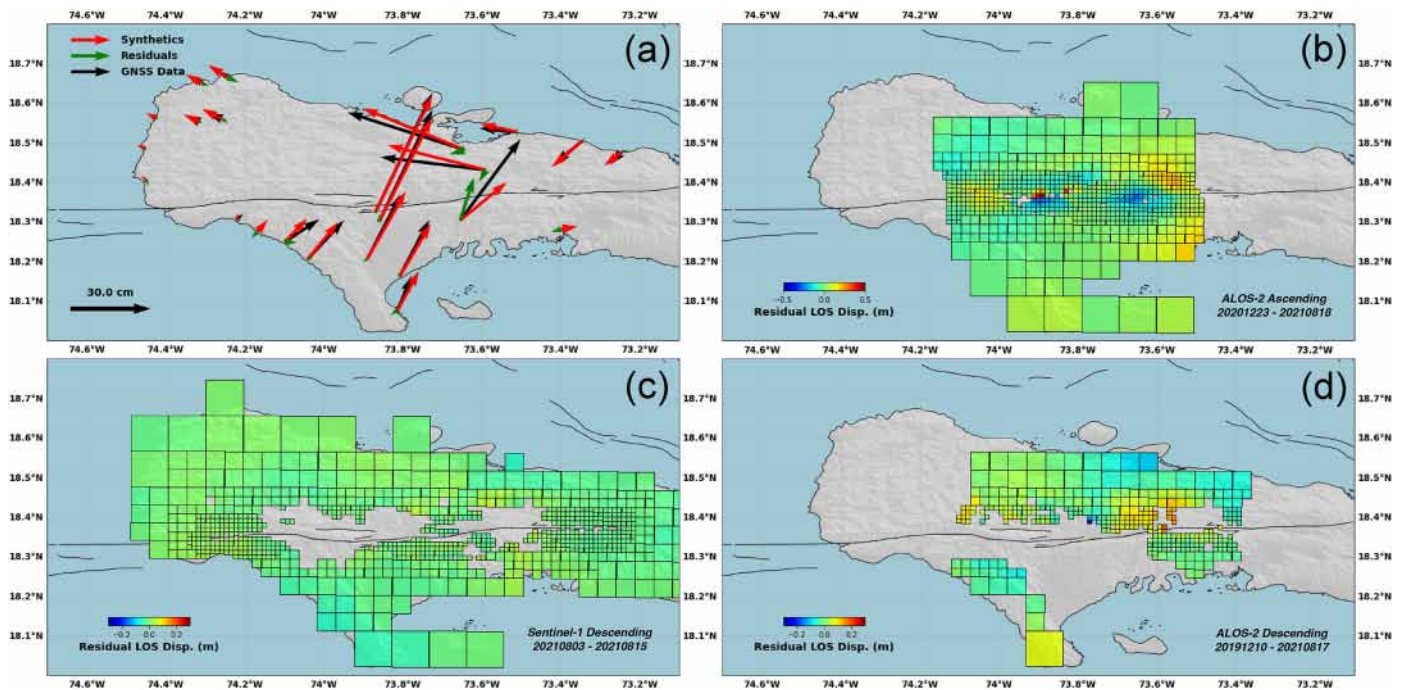


Figure 4. (a) Black arrows are Global Navigation Satellite System-derived coseismic displacements. Red arrows are predicted coseismic displacement from the preferred slip model. Green arrows are residuals, difference between the modeled and observed surface displacement. (b) Residuals along the ALOS-2 ascending track 43. (c) Residuals along the Sentinel-1 descending track 142. (d) Residuals along the ALOS-2 descending track 138. Interferometric Synthetic Aperture Radar residuals are the difference between the model prediction and the geodetic data in the satellite line of sight. Larger residuals are observed in the area where post-seismic afterslip has been described and might influence the most our solution.

moment on the RSF segment. This estimated seismic moment release, indicative of dual strike-slip/dip-slip release on the north-dipping thrust but dominantly strike-slip on the RSF, is consistent with the geodetic observations that indicate vertical motion near the north-dipping thrust and mainly horizontal motion to the west.

4. Discussion

4.1. Interseismic Build-Up and Coseismic Release

Since earthquakes at plate boundaries release the slip deficit that builds up during the interseismic period, the corresponding stress release should reflect the ambient, that is, long-term, regional tectonic stress field. Early GNSS analyses in southern Haiti show a velocity gradient indicative of a locked EPGF system with a slip deficit building up at a rate of 7 ± 2 mm.yr⁻¹ (Calais et al., 2010; Manaker et al., 2008), consistent with the to 9 ± 2 mm.yr⁻¹ rate later derived from paleoseismology (Saint Fleur et al., 2019). These studies however focused on the strike-slip component of motion between the Gonave microplate and the Caribbean plate. Subsequent offshore mapping show a system of reverse faults and folds along the northern coast of the Southern Peninsula and further north in the Gonave Gulf, indicative of an additional component of plate boundary-normal shortening (Aiken et al., 2016; Corbeau et al., 2016). Interestingly, a kinematic block model constrained by GNSS-derived velocities (Benford et al., 2012) predicts oblique motion on the supposedly purely strike-slip EPGF system, with fault-normal convergence of comparable amplitude to the fault-parallel motion. Plate boundary-normal shortening is also documented further east along the Cul-de-Sac and Enriquillo basins through geological (Saint Fleur et al., 2019), geodetic (Symithe & Calais, 2016), and seismological (Rodriguez et al., 2018) investigations.

The most recent GNSS analysis (Calais, Symithe, & de Lépinay, 2022) confirms that the motion between the Gonave microplate and the Caribbean plate is partitioned between strike-slip on the EPGF system and shortening mostly focused on the reverse fault system that runs offshore along the northern coast of the Southern Peninsula, which was partly activated during the aftershock sequence of the 2010 Léogâne earthquake along the Trois Baies segment (Douilly et al., 2013; Symithe et al., 2013). Therefore, the mode of strain build-up in southern Haiti combines plate boundary-normal shortening and plate boundary-parallel strike-slip. Calais et al. (2010) showed

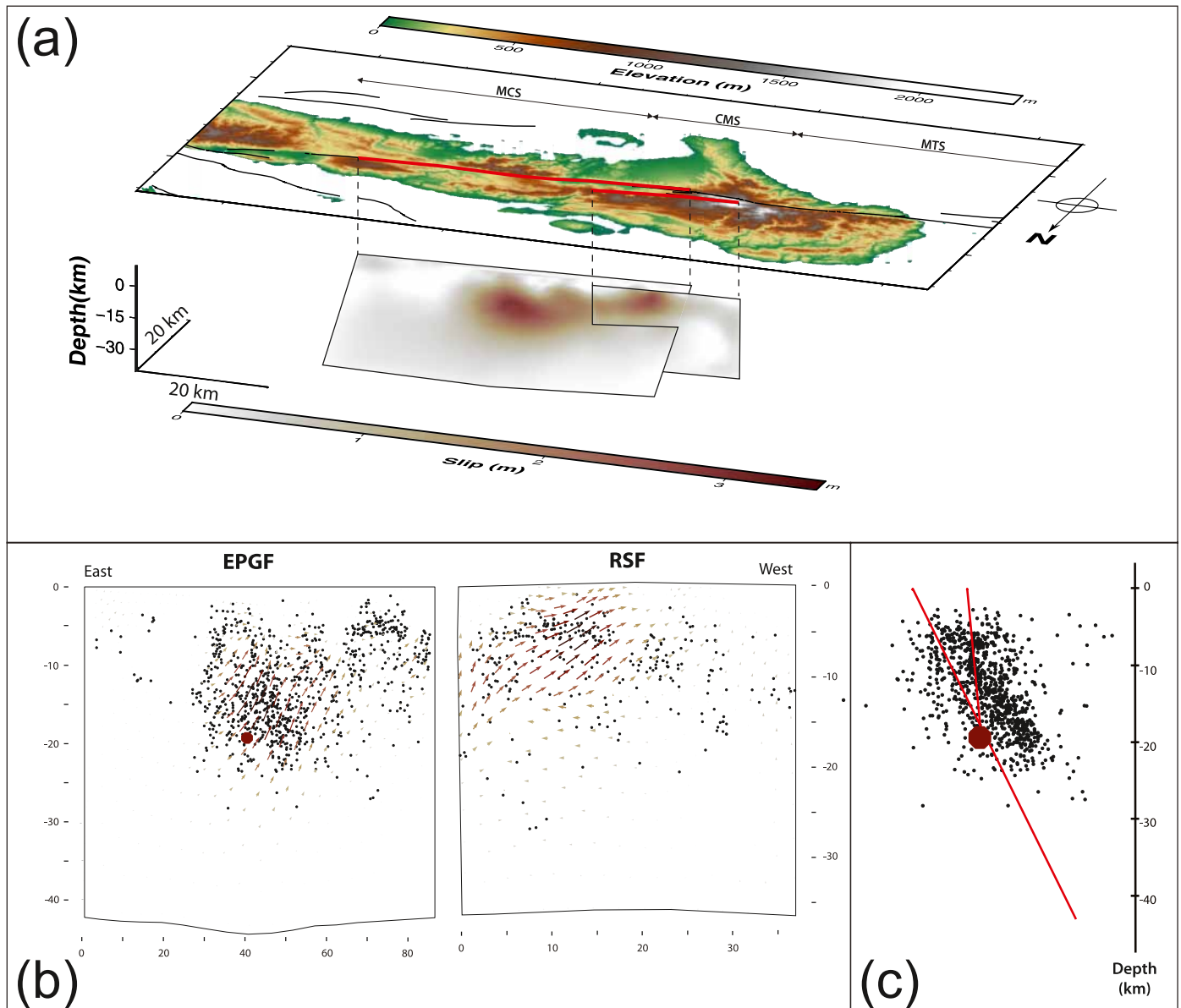


Figure 5. (a) 3D geometry of the preferred coseismic slip model, viewed from the north-west of the Southern Peninsula and showing the two segments described in the text. The north-dipping thrust in the east dips at $66 \pm 4^\circ$ while the RSF segment to the west is close to vertical, with a steep northward dip angle of $86 \pm 2^\circ$. Black lines are the surface projection of the modeled faults. Fault segmentation proposed by Saint Fleur et al. (2020) is shown, with MTS: Macaya-Tiburon Segment, CMS: Clonard-Macaya Segment, MCS: Miragoâne-Clonard Segment. (b) (left) North-dipping thrust slip model from the best fitting geometry, with slip vectors representing the direction of coseismic slip. (right) RSF slip model from the best fitting geometry, with slip vectors representing the direction of slip. Black dots are relocated aftershocks from a first month post-rupture subset from the analysis of (Douilly et al., 2022). The mainshock of the Nippes earthquakes is represented by the darkred octagon. (c) Cross-section within the main rupture. The main ruptured fault is depicted in red and the darkred octagon indicate the mainshock localization from Calais, Symithe, Monfret, et al. (2022). Aftershocks are the same as in panel (b).

that the moment release during the 2010 Léogâne earthquake was 62% strike-slip and 38% by reverse, a result very similar to the one found here for 2021 Nippes earthquake. We therefore observe consistency between strain release during the 2010 and 2021 earthquakes and interseismic strain build-up in southern Haiti, with both events releasing part of this elastic strain via a combination of thrusting and strike slip faulting.

That the 2010 Mw 7.0 and 2021 Mw 7.2 earthquakes ruptured with a combined mechanism does not preclude the possibility of a rupture of the main EPGF. Paleoseismological evidence show that this must have been the case, even though no reliable dating of these events is yet available (Saint Fleur et al., 2020). Martin and Hough (2022)

also propose that the 8 April 1860, earthquake near the city of Anse-à-Veau (M6.8) ruptured the EPGF, on the basis of historical archives of damage descriptions. Conversely, large and purely strike-slip earthquakes on the relatively long segments of the EPGF system (Saint Fleur et al., 2019) may actually be rare because of the slow tectonic loading of the fault. The transpressional interseismic stress regime may indeed favor the initial rupture of reverse faults, secondary and oblique to the EPGF, but well-oriented within the regional stress field.

4.2. Did the Earthquake Rupture the EPGF Itself?

The analogies between the 14 August 2021, Mw 7.2 earthquake and its 12 January 2010, Mw 7.0 predecessor are striking. Both occurred in the close vicinity of the EPGF and included a significant amount of reverse coseismic slip in a context where pure strike-slip motion was initially expected. Both initiated with oblique slip on a north-dipping eastern fault segment, then propagated westward with mostly left-lateral strike-slip. In 2010, the inversion of geodetic data (Calais et al., 2010; Hayes et al., 2010) showed that the rupture involved a fault which is not the main EPGF, a result later confirmed by a detailed analysis of the spatial distribution of aftershocks (Douilly et al., 2013). This was however challenged by Saint Fleur et al. (2019) who proposed a rupture of the main EPGF, though with a geometry that is not consistent with the distribution of aftershock.

That a smaller fault, secondary to the major plate boundary fault, ruptures in a moderate magnitude earthquake is not uncommon. For instance, the 1989, Mw 6.9, Loma Prieta earthquake in northern California ruptured a steeply dipping thrust fault subparallel to the San Andreas fault but only 5 km away from the main fault trace (Beroza, 1991; Dietz & Ellsworth, 1990; Kilb et al., 1997). The 2003, Mw 6.5 San Simeon earthquake occurred on the Oceanic thrust fault, 60 km west of the main trace of the San Andreas fault in the Coastal Ranges of central California (McLaren et al., 2008). In fact, no significant earthquake in California since the 1906 San Francisco earthquake ruptured the main San Andreas Fault. All large earthquakes occurred on secondary structures, except for the Parkfield earthquakes (e.g., 1857, 1966, and 2004).

In the case of the 2021 Nippes earthquake, the InSAR data and the aftershock distribution show that the rupture involved the RSF segment to the west, a short fault segment parallel to—but distinct from—the EPGF. In its eastern part, geodetic inversions shown here and an early analysis of the aftershock distribution (Calais, Symithe, Monfret, et al., 2022) are both consistent with the rupture of a N- to NNE-dipping fault segment slightly oblique to the direction of the EPGF, but that may merge with it toward the surface. As no direct observation exists of the actual dip of the EPGF throughout the Southern Peninsula of Haiti, we cannot determine whether the eastern part of the rupture involved the EPGF proper. However, offshore seismic data to the west of the Southern Peninsula in the Jamaica Passage show quite clearly that the EPGF is indeed a vertical fault, locally associated with secondary compressional structures such as pressure ridges, restraining bends, or step overs (Leroy et al., 2015). Also, a study of triggered tremors in the Southern Peninsula following the 27 February 2010 Mw8.8 Maule earthquake hints that the EPGF may rather be steeply dipping to the south, opposite to the ruptures imaged geodetically in 2010 and 2021 (Aiken et al., 2016). Finally, Douilly et al. (2022) found triggered aftershocks on two vertically distributed clusters, off the main north-dipping earthquake rupture, which likely occurred on the main EPGF. This is an indication that the EPGF may be close to vertical and therefore distinct from the 14 August 2021, rupture. More work on the precise relocation of aftershocks will likely shed new light on the geometry of the EPGF at depth.

4.3. Aftershocks Location Versus Coseismic Slip Distribution

Earthquake ruptures generate static and dynamic stress changes that alter fault zone properties and may bring faults and bulk material closer to—or farther away from—failure (Gomberg et al., 1998; Kilb et al., 2000). Aftershocks tend to coincide with areas of large stress changes in the medium, in areas where slip varies sharply in space, such as around the edges of the main coseismic slip patches, at fault terminations, or at high-to-low slip transition areas (Das & Henry, 2003; Stein, 1999; Wetzler et al., 2018). In some cases, such as the 1996 Biak subduction earthquake (Henry & Das, 2002), aftershocks concentrate close to the rupture, coinciding with high coseismic slip areas. However, there does not appear to be a universal relation between high- and low-slip areas and high or low aftershock occurrence (Das & Henry, 2003). Recent studies also show that afterslip can trigger aftershocks as stress within the fault area experiencing afterslip grows with time until some critical value (Perfettini & Avouac, 2004, 2007; Perfettini et al., 2018). Afterslip-driven aftershocks are therefore expected to surround the main co-seismic slip patches (Avouac, 2015).

We now compare the precise aftershock locations from Douilly et al. (2022) based on a network of 12 broadband seismic stations deployed in the epicentral area within a week of the earthquake, with our preferred slip model. To first order, aftershocks of the 2021 Nippes earthquake appear to largely overlap areas of largest coseismic slip, as shown on Figure 5b. The distribution of aftershocks between 73.45° and 73.7°W, in the vicinity of the main fault plane, show two clusters with different strike angles. A first one strikes ~270°N, which is compatible with some aftershocks occurring on the rupture. A second cluster strikes ~150°N, which is compatible with activated high dip angles antithetic faults in the hanging wall (Ronald et al., 1973).

This is also visible in the cross-section on Figure 5c, which shows that a large number of aftershocks are located off-fault and in the hanging wall of the ruptured segments. This is similar to the 2010 Léogâne earthquake further east (Douilly et al., 2013), where the bulk of the aftershocks occurred in the vicinity of the two areas of larger coseismic slip, and were mostly located in the hanging wall of the rupture.

Aftershock activity in the volume surrounding the rupture, mostly above it, was also observed after the 2016 Pedernales (Agurto-Detzel et al., 2019) and 1994 Northridge (Thio & Kanamori, 1996) earthquakes, for instance. Oglesby et al. (1998) and Oglesby et al. (2000) computed dynamic models of dip-slip ruptures and showed that the hanging wall experiences significantly larger acceleration than the footwall because of (a) its lower mass compared to the foot-wall, and (b) the stress field interaction with the free surface. These larger accelerations result in more damage in the hanging wall, which could explain the preferential occurrence of aftershocks above the rupture (Gabuchian et al., 2017). Also, Lin and Stein (2004) modeled Coulomb stress changes on a thrust fault and found the largest stress changes in the hanging wall of the rupture, a potential explanation for off-fault aftershocks.

We performed Coulomb stress changes calculations (Lin & Stein, 2004; Toda et al., 2005) using only the north-dipping thrust slip model and find static stress increases in the close vicinity of the RSF which could have promoted rupture of the RSF, consistently with Okuwaki and Fan (2022). That said, dynamic stress changes are overwhelmingly dominant during rupture propagation and need to be taken into account. We compute Coulomb stress changes with the coseismic slip model described above and receiver faults striking N150/N270, with a dip angle of 75°/80°, and a rake angle of 120°/250° (Figure 6). We use mean values of rake and dip angles from the aftershocks of Douilly et al. (2022) in each striking cluster. We find a volume of increased Coulomb stress in the hanging-wall of the rupture that matches well the distribution of aftershocks shown on Figure 5c. It is therefore possible that some of the aftershocks observed in the hanging-wall of the Nippes earthquake rupture were triggered by coseismic Coulomb stress changes.

Indeed, the detailed interferometric study of Yin et al. (2022) shows the postseismic activation of off-rupture faults in the weeks following the earthquake. They are mostly located to the north of the rupture and often coincide with known geological faults. We hence propose that off-fault damage in the hanging wall of the rupture results from the combination of coseismic slip distribution and rupture geometry, which favor the activation of pre-existing secondary faults.

4.4. Segmentation of the EPGF System and Associated Earthquake Potential

Large strike-slip faults may rupture in long earthquakes, up to several hundreds of kilometers long, as for instance the 2001 Kokoxili Mw 7.8 earthquake which ruptured a 450-km-long portion of the Kunlun strike-slip fault (Klinger, 2010; Klinger et al., 2005; Lasserre et al., 2005). The EPGF is a 300 km-long continental fault with an offshore continuation up-to 1,100 km-long west of the Jamaica Passage. The system is known to accumulate strain over the years as expressed by historical seismicity (Bakun et al., 2012; Prentice et al., 2010; Scherer, 1912; Tabrez et al., 2008, Figure 1a) and geodetic data (Symithe et al., 2015). Following scaling laws, a rupture of the whole EPGF on-land would generate a Mw > 8 earthquake. Still, the fault system has only ruptured in 2021 and 2010 in Mw 7 events involving secondary structures (e.g., Léogâne Fault for 2010 and Ravine du Sud for 2021) with uncertainties about the rupture of the EPGF fault in 2021.

Two hypotheses must then be considered. First, let us assume the faults that ruptured during the 2021 earthquake did not involve the main EPGF. The rupture of secondary faults adjacent to a main fault system is a common behavior of continental strike-slip faults (e.g., San Andreas, North Anatolian) (Klinger, 2010; Kondo et al., 2005; Segall & Pollard, 1980; Wesnousky, 2006). In addition, ruptures on structures adjacent to major faults can also propagate to the main fault system, and inversely, as for the 2001 Kokoxili earthquake which nucleated on the

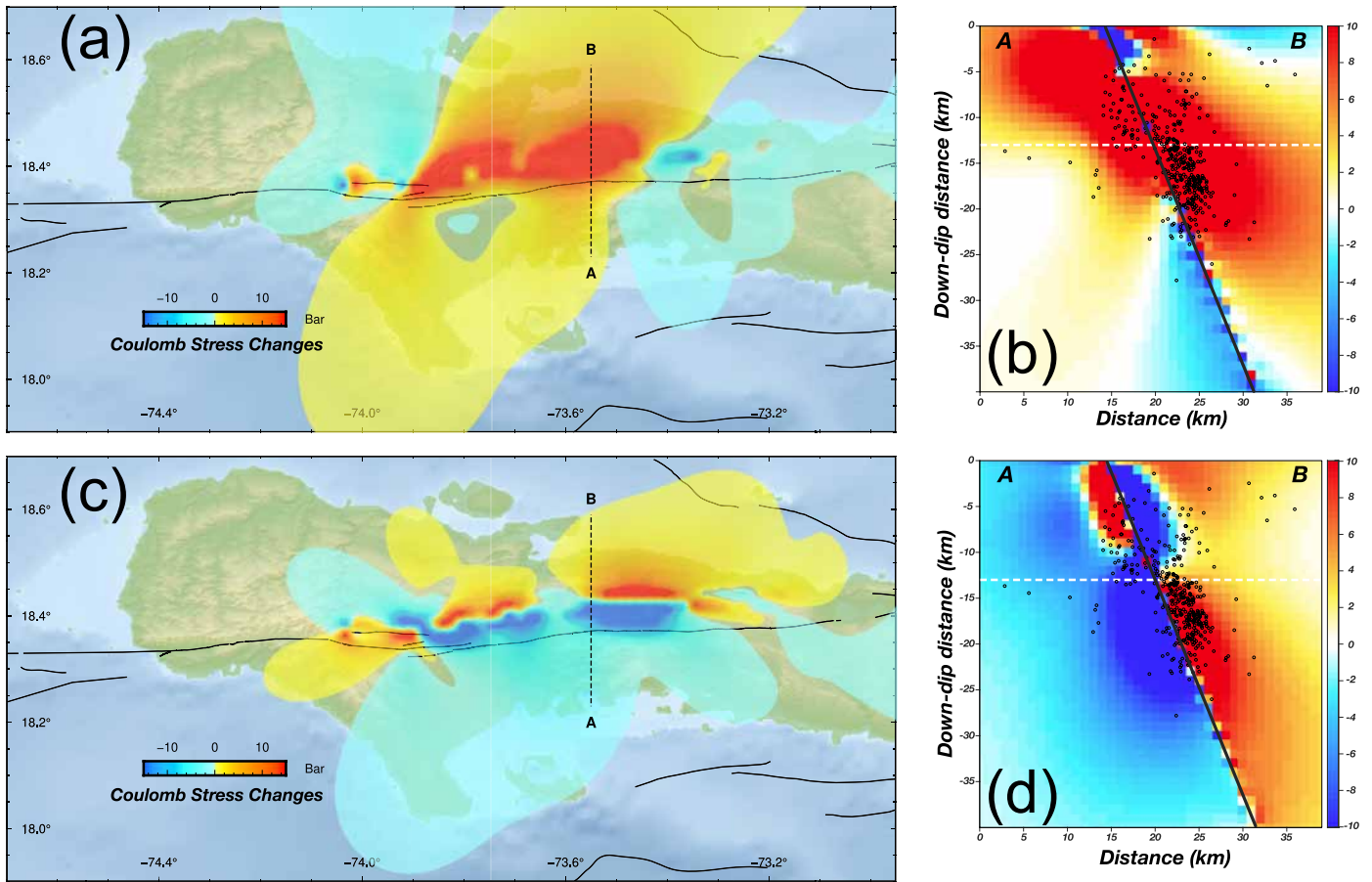


Figure 6. (a) Coulomb stress changes derived from model in Figure S16 of Supporting Information S1 for a receiver fault striking 270°N , dipping $\text{N}80^{\circ}$ and with a 250° rake angle at a depth of 13 km. Coulomb stress changes values are in bars. Receiver fault parameters comes from the analysis of the study of Douilly et al. (2022). (b) Cross-section A-B from the Coulomb stress changes calculation on panel (a). The Coulomb stress map on panel (a) is situated on the white dashed line. First month post-rupture subset of the aftershocks from Douilly et al. (2022) within 15 km distance from the profile are represented projected. (c) Coulomb stress changes derived from model in Figure S16 of Supporting Information S1 for a receiver fault striking 150°N , dipping $\text{SW-}75^{\circ}$ and with a 120° rake angle at a depth of 13 km. Coulomb stress changes values are in bars. Receiver fault parameters comes from the analysis of the study of Douilly et al. (2022). (d) Cross-section A-B from the Coulomb stress changes calculation on panel (c). The Coulomb stress map on panel (c) is situated on the white dashed line. First month post-rupture subset of the aftershocks from Douilly et al. (2022) within 15 km distance from the profile are represented projected.

Heituo fault before joining the main Kunlun fault (Lasserre et al., 2005). Mechanisms in which secondary faults rupture preferably to the main fault system could explain the observed EPGF system behavior, with very rare $M_w > 8$ events rupturing the EPGF while most of the accommodated strain is released by secondary structures rupturing more often in $M_w \sim 7$ events.

Second, let us assume that the 2021 rupture actually involved the EPGF, and that segmentation played a role in the rupture propagation. In addition to secondary structures, fault segmentation is a well-known feature of major continental strike-slip fault and may result in complex coseismic slip distributions (e.g., Klinger, 2010). Series of segmented faults and especially their associated geometrical complexities (e.g., azimuth changes, step-overs, bends and relay zones or jogs) are important factors in the earthquake rupture dynamics (nucleation, propagation, termination) (Klinger, 2010; Wesnousky, 2006). Discontinuities and variability along strike can therefore delay or advance rupture propagation limiting the length of earthquake rupture.

The EPGF system has only ruptured a small section of ~ 60 km between L'Asile to the east and Pic Macaya to the west in 2021 and a section of ~ 40 km segment in 2010 between Grand Goâve and Petion-Ville. Both the 2010 and 2021 events do not present major geometrical asperities or discontinuities in their surface expression except at their terminations. The EPGF azimuth changes of $\sim 5^{\circ}$ along the Clonard basin, an azimuth change large enough to delimit a segment that ruptured in 2021 (King & Nábělek, 1985; Saint Fleur et al., 2020; Wesnousky, 2006).

Klinger (2010) also notes that segments of continental strike-slip faults are limited in size, reaching a maximum of approximately 25 km. We mapped slip on the rupture over an approximately 25 km-long segment, which could therefore explain why the rupture jumped into another segment to the west. Then, fault steps and bends that build the topographic Pic Macaya feature may have affected the dynamics of the rupture and could have stopped the 2021 event. This segmentation is coherent with the fault mapping described by Saint Fleur et al. (2020) (Figure 5a).

In conclusion, both hypothesis suggest an important role of fault segmentation in the dynamics of stress release along the EPGF system, with significant implications on seismic hazard assessment.

Now, whether the EPGF ruptured during the main 2021 earthquake or not, it is important to assess how such apparent segmentation might modify our understanding of the seismogenic behavior of the EPGF. Envisioning the EPGF as a segmented system changes our understanding about the way this fault system may rupture. On one side, the EPGF is viewed as a long strike-slip continental fault accumulating stress at depth which could rupture in $M_w > 8$ earthquakes (Manaker et al., 2008). On the other hand, if segmented, the EPGF might break into a series of more earthquakes of fewer magnitudes, although the synchronous rupture of all segments cannot be excluded.

From our study, we propose that EPGF is segmented, at least within the first 15 km at depth. Over the whole EPGF system, several fault segments ruptured in ~ 11.5 years. Benford et al. (2012) proposed that a sequence of cascading earthquakes, in 1701, 1751, 1770, and 1860, released strain that accumulated beforehand (Bakun et al., 2012; Martin & Hough, 2022; Saint Fleur et al., 2020). Tabrez et al. (2008) also show from Coulomb stress changes calculation that coseismic stress changes in the area of the 2010 event are prone to increase cascading events along the EPGF system. We might be experiencing such cascade of events, both controlled by the segmentation of the EPGF and by stress redistribution left in the wake of each large event. Mapping the EPGF system at the surface and at depth and deciphering the possible lateral segmentation of the faults is therefore a key factor for seismic hazard analyses over Hispaniola.

5. Conclusion

We use surface displacement data from InSAR and near-field GNSS measurements to determine the rupture geometry and coseismic slip distribution of the 2021 Nippes earthquake. Consistently with previous studies, we find that the earthquake involved a combination of thrust and strike-slip motion, resulting in an overall transpressional mechanism bearing similarities with the 12 January 2010 events further east. The rupture mechanisms of the 2010 and 2021 earthquakes are consistent with the interseismic accumulation of transpressional strain within the Southern Peninsula and just to the north of it, offshore. It therefore appears that the plate boundary-normal shortening component recently observed in various geophysical and geological data sets, superimposed on the long-known left-lateral strike-slip component, is seismically released in southern Haiti.

The coseismic offsets derived from GNSS and InSAR data are consistent with a two-segment slip model and do not require a more complex geometry to fit the data within their uncertainties. We find that the data is well fit by the rupture of (a) a north-dipping segment in the east, with a dip angle of $66 \pm 4^\circ$ that released 40% of thrust moment and 60% of strike-slip moment and (b) a quasi-vertical western segment with a dip angle of $86 \pm 2^\circ$ that dominantly released strike-slip moment. The latter segments coincides with the Ravine du Sud fault, while the former one may coincide with the EPGF, though more data is needed to ascertain this interpretation.

Distribution of aftershocks versus slip distribution indicates a complex distribution of remaining stresses in the hanging wall associated with possible frictional heterogeneities along the fault zone following the mainshock. Aftershocks following the Nippes event are more likely coseismically induced and caused by damage within the rock volume above the rupture. Off-fault damage in the hanging-wall and associated aftershocks may have been favored by the activation of pre-existing secondary faults (Yin et al., 2022).

Current seismic hazard maps for Haiti of Frankel et al. (2011) assume that the Gonave-Caribbean relative plate motion is accommodated by pure strike-slip on a vertical fault. The 2010 and 2021 transpressional earthquakes of southern Haiti, as well as the interseismic GNSS velocities, show that a significant component of plate boundary-normal shortening that is not accounted for in the current hazard estimates. Also, these calculations assume seismic strain release on a single vertical EPGF, whereas these recent events show a segmented fault

system, with ruptures on non-vertical faults off the EPGF. This indicates that an update of the regional seismic hazard maps is required in order to account for such transpressional mode of strain release.

Data Availability Statement

GNSS coseismic displacements are listed in the Supplementary Materials, and archived at Rimbault et al. (2022), together with InSAR displacements data and GNSS interseismic velocities. Aftershocks datasets used in this study are available in the supplementaries from the study of Calais, Smithe, Monfret, et al. (2022) and Douilly et al. (2022) and on the Ayiti-Séismes platform (<https://ayiti.unice.fr/ayiti-seismes>). Fault traces come from the study of Saint Fleur et al. (2019). We use Copernicus data from the Sentinel-1AB satellites provided by the European Space Agency (ESA, <https://scihub.copernicus.eu>). The ALOS-2 data were provided by the Japan Aerospace Exploration Agency (JAXA) through the Earthquake Working Group for the Evaluation of ALOS and ALOS-2 for Use in Disaster Mitigation, coordinated by the Geospatial Information Authority of Japan (GSI) and JAXA. JAXA conducted emergency observations immediately after the earthquake. The processing of interferograms was made with ISCE2 (<https://github.com/isce-framework/isce2>). Shuttle Radar Topography Mission (SRTM) 1 Arc-Second Global data was retrieved from <https://doi.org/10.5066/F7K072R7>. Centroid Moment Tensors were obtained from the Global CMT web page (<https://www.globalcmt.org>). Some figures were created with Python Generic Mapping Tool (PyGMT) (<https://www.pygmt.org/>, Uieda et al., 2022) and matplotlib (<https://matplotlib.org>, Hunter, 2007). ERA-5 global reanalyses of atmospheric data are distributed by the ECMWF on the Climate Datastore platform (<https://cds.climate.copernicus.eu>). PyAPS (<https://github.com/insarlab/PyAPS>) was used to calculate tropospheric delays. Coulomb3 software (Lin & Stein, 2004; Toda et al., 2005) to compute the Coulomb stress changes. Classic Slip Inversion (CSI) package was used for the inversion, plot and handling of the geodetic data (<https://github.com/jolivet/csi>).

Acknowledgments

This work received funding from the European Research Council under the European Union's Horizon 2020 research and innovation program (Geo-4D project, Grant agreement 758210). RJ and EC acknowledge funding from the Institut Universitaire de France. Funding to SJS for the 2017–2018 GNSS measurement campaigns in Haiti was provided by Geosciences Without Borders. Funding to EC for the 2018–2020 GNSS campaigns in Haiti was provided by the FEDER European Community program within the Interreg Caraïbes “PREST” project. This paper uses services provided by the GAGE Facility, operated by UNAVCO, Inc., with support from the National Science Foundation, the National Aeronautics and Space Administration, and the U.S. Geological Survey under NSF Cooperative Agreement EAR-1724794. We are particularly thankful to G. Mattioli and his group at UNAVCO for quickly providing the GNSS equipment necessary to measure coseismic displacements. We acknowledge support from the Haiti National Center for Geospatial Information for providing access to data from their continuously operating GNSS stations. We thank the Haiti Bureau of Mines and Energy for their rapid deployment of GNSS instruments after the earthquake in a context where access to the field was complicated by social insecurity. We also thank the editor for handling the manuscript and Pr. Gareth Funning and one anonymous reviewer for providing suggestions that improved the manuscript.

References

- Agurto-Detzel, H., Font, Y., Charvis, P., Régner, M., Rietbrock, A., Ambrosio, D., et al. (2019). Ridge subduction and afterslip control after-shock distribution of the 2016 Mw 7.8 Ecuador earthquake. *Earth and Planetary Science Letters*, 520, 63–76. <https://doi.org/10.1016/j.epsl.2019.05.029>
- Aiken, C., Chao, K., Gonzalez-Huizar, H., Douilly, R., Peng, Z., Deschamps, A., et al. (2016). Exploration of remote triggering: A survey of multiple fault structures in Haiti. *Earth and Planetary Science Letters*, 455, 14–24. <https://doi.org/10.1016/j.epsl.2016.09.023>
- Altamimi, Z., Rebischung, P., Métivier, L., & Collilieux, X. (2016). ITRF2014: A new release of the International Terrestrial Reference Frame modeling nonlinear station motions. *Journal of Geophysical Research-Solid Earth*, 121(8), 6109–6131. <https://doi.org/10.1002/2016JB013098>
- Avouac, J.-P. (2015). From geodetic imaging of seismic and aseismic fault slip to dynamic modeling of the seismic cycle. *Annual Review of Earth and Planetary Sciences*, 43(1), 233–271. <https://doi.org/10.1146/annurev-earth-060614-105302>
- Bakun, W. H., Flores, C. H., & ten Brink, U. S. (2012). Significant earthquakes on the Enriquillo Fault System, Hispaniola, 1500–2010: Implications for seismic hazard. *Bulletin of the Seismological Society of America*, 102(1), 18–30. <https://doi.org/10.1785/0120110077>
- Baran, I., Stewart, M., Kampes, B., Perski, Z., & Lilly, P. (2003). A modification to the Goldstein radar interferogram filter. *IEEE Transactions on Geoscience and Remote Sensing*, 41(9), 2114–2118. <https://doi.org/10.1109/TGRS.2003.817212>
- Benford, B., DeMets, C., & Calais, E. (2012). GPS estimates of microplate motions, northern Caribbean: Evidence for a Hispaniola microplate and implications for earthquake hazard. *Geophysical Journal International*, 191(2), 481–490. <https://doi.org/10.1111/j.1365-246X.2012.05662.x>
- Beroza, G. C. (1991). Near-source modeling of the Loma Prieta earthquake: Evidence for heterogeneous slip and implications for earthquake hazard. *Bulletin of the Seismological Society of America*, 81(5), 1603–1621.
- Calais, E., Freed, A., Mattioli, G., Amelung, F., Sigurjón, J., Jansma, P., et al. (2010). Transpressional rupture of an unmapped fault during the 2010 Haiti earthquake. *Nature Geoscience*, 3(11), 1–6. <https://doi.org/10.1038/ngeo992>
- Calais, E., Smithe, S., Mercier de Lépinay, B., & Prépetit, C. (2016). Plate boundary segmentation in the northeastern Caribbean from geodetic measurements and Neogene geological observations. *Comptes Rendus Geoscience*, 348(1), 42–51. <https://doi.org/10.1016/j.crte.2015.10.007>
- Calais, E., Smithe, S. J., & de Lépinay, B. M. (2022). Strain partitioning within the Caribbean–North America transform plate boundary in southern Haiti, tectonic and hazard implications. *Bulletin of the Seismological Society of America*, 113(1), 131–142. <https://doi.org/10.1785/0120220121>
- Calais, E., Smithe, S. J., Monfret, T., Delouis, B., Lomax, A., Courboux, F., et al. (2022). Citizen seismology helps decipher the 2021 Haiti earthquake. *Science*, 376(6590), 283–287. <https://doi.org/10.1126/science.abn1045>
- Chen, C., & Zebker, H. (2002). Phase unwrapping for large SAR interferograms: Statistical segmentation and generalized network models. *IEEE Transactions on Geoscience and Remote Sensing*, 40(8), 1709–1719. <https://doi.org/10.1109/TGRS.2002.802453>
- Corbeau, J., Rolandone, F., Leroy, S., Meyer, B., Mercier de Lépinay, B., Ellouz-Zimmermann, N., & Momplaisir, R. (2016). How transpressive is the northern Caribbean plate boundary? *Tectonics*, 35(4), 1032–1046. <https://doi.org/10.1002/2015TC003996>
- Das, S., & Henry, C. (2003). Spatial relation between main earthquake slip and its aftershock distribution. *Reviews of Geophysics*, 41(3), 1013. <https://doi.org/10.1029/2002RG000119>
- DeMets, C., Jansma, P. E., Mattioli, G. S., Dixon, T. H., Farina, F., Bilham, R., et al. (2000). GPS geodetic constraints on Caribbean–North America plate motion. *Geophysical Research Letters*, 27(3), 437–440. <https://doi.org/10.1029/1999GL005436>
- Dietz, L. D., & Ellsworth, W. L. (1990). The October 17, 1989, Loma Prieta, California, earthquake and its aftershocks: Geometry of the sequence from high-resolution locations. *Geophysical Research Letters*, 17(9), 1417–1420. <https://doi.org/10.1029/GL017i009p01417>
- Douilly, R., Ellsworth, W. L., Kissling, E., Freed, A. M., Deschamps, A., & Mercier de Lépinay, B. (2016). 3-D velocity structure in southern Haiti from local earthquake tomography. *Journal of Geophysical Research: Solid Earth*, 121(12), 8813–8832. <https://doi.org/10.1002/2016JB013123>

- Douilly, R., Haase, J. S., Ellsworth, W. L., Bouin, M., Calais, E., Symithe, S. J., et al. (2013). Crustal structure and fault geometry of the 2010 Haiti earthquake from temporary seismometer deployments. *Bulletin of the Seismological Society of America*, 103(4), 2305–2325. <https://doi.org/10.1785/0120120303>
- Douilly, R., Paul, S., Monfret, T., Deschamps, A., Ambrois, D., Symithe, S. J., et al. (2022). Rupture segmentation of the 14 August 2021 Mw 7.2 Nippes, Haiti, earthquake using aftershock relocation from a local seismic deployment. *Bulletin of the Seismological Society of America*, 10(1), 58–72. <https://doi.org/10.1785/0120220128>
- Elliott, J. R., Jolivet, R., González, P. J., Avouac, J. P., Hollingsworth, J., Searle, M. P., & Stevens, V. L. (2016). Himalayan megathrust geometry and relation to topography revealed by the Gorkha earthquake. *Nature Geoscience*, 9(2), 174–180. <https://doi.org/10.1038/ngeo2623>
- Farr, T. G., Rosen, P. A., Caro, E., Crippen, R., Duren, R., Hensley, S., et al. (2007). The Shuttle radar topography mission. *Reviews of Geophysics*, 45(2), RG2004. <https://doi.org/10.1029/2005RG000183>
- Fattahi, H., Agram, P., & Simons, M. (2016). A network-based enhanced spectral diversity approach for TOPS time-series analysis. *IEEE Transactions on Geoscience and Remote Sensing*, 55(2), 1–10. <https://doi.org/10.1109/TGRS.2016.2614925>
- Frankel, A., Harmsen, S., Mueller, C., Calais, E., & Haase, J. (2011). Seismic hazard maps for Haiti. *Earthquake Spectra*, 27(1), 23–41. <https://doi.org/10.1193/1.3631016>
- Gabuchian, V., Rosakis, A. J., Madariaga, R., Kanamori, H., & Bhat, H. S. (2017). Experimental evidence that thrust earthquake ruptures might open faults. *Nature*, 545(7654), 1–5. <https://doi.org/10.1038/nature22045>
- Goldstein, R. M., & Werner, C. L. (1998). Radar interferogram filtering for geophysical applications. *Geophysical Research Letters*, 25(21), 4035–4038. <https://doi.org/10.1029/1998GL900033>
- Gomberg, J., Beeler, N. M., Blanpied, M. L., & Bodin, P. (1998). Earthquake triggering by transient and static deformations. *Journal of Geophysical Research*, 103(B10), 24411–24426. <https://doi.org/10.1029/98JB01125>
- Hayes, G. P., Briggs, R. W., Sladen, A., Fielding, E. J., Prentice, C., Hudnut, K., et al. (2010). Complex rupture during the 12 January 2010 Haiti earthquake. *Nature Geoscience*, 3(11), 800–805. <https://doi.org/10.1038/ngeo977>
- Henry, C., & Das, S. (2002). The Mw 8.2 17 February 1996 Biak Indonesia, earthquake: Rupture history, aftershocks, and fault plane properties. *Journal of Geophysical Research*, 107(B11), ESE 11-1–ESE 11-16. <https://doi.org/10.1029/2001JB000796>
- Herring, T., King, R., & McClusky, S. (2010). *Introduction to GAMIT/GLOBK*. Massachusetts Institute of Technology.
- Hunter, J. D. (2007). Matplotlib: A 2D graphics environment. *Computing in Science & Engineering*, 9(3), 90–95. <https://doi.org/10.1109/MCSE.2007.55>
- Jarvis, A., Reuter, H., Nelson, A., & Guevara, E. (2008). Hole-filled SRTM for the globe Version 4, available from the CGIAR-CSI SRTM 90m database. Retrieved from <http://srtm.csi.cgiar.org>
- Jolivet, R., Agram, P. S., Lin, N. Y., Simons, M., Doin, M.-P., Peltzer, G., & Li, Z. (2014a). Improving InSAR geodesy using global atmospheric models. *Journal of Geophysical Research-Solid Earth*, 119(3), 2324–2341. <https://doi.org/10.1002/2013JB010588>
- Jolivet, R., Duputel, Z., Riel, B., Simons, M., Rivera, L., Minson, S. E., et al. (2014b). The 2013 Mw 7.7 Balochistan earthquake: Seismic potential of an accretionary wedge. *Bulletin of the Seismological Society of America*, 104(2), 1020–1030. <https://doi.org/10.1785/0120130313>
- Jolivet, R., Grandin, R., Lasserre, C., Doin, M. P., & Peltzer, G. (2011). Systematic InSAR tropospheric phase delay corrections from global meteorological reanalysis data. *Geophysical Research Letters*, 38(17), L17311. <https://doi.org/10.1029/2011GL048757>
- Jolivet, R., Lasserre, C., Doin, M. P., Guillaso, S., Peltzer, G., Dailu, R., et al. (2012). Shallow creep on the Haiyuan fault (Gansu, China) revealed by SAR interferometry. *Journal of Geophysical Research*, 117(B6), B06401. <https://doi.org/10.1029/2011JB008732>
- Jolivet, R., Simons, M., Agram, P. S., Duputel, Z., & Shen, Z. K. (2015). Aseismic slip and seismogenic coupling along the central San Andreas Fault. *Geophysical Research Letters*, 42(2), 297–306. <https://doi.org/10.1002/2014GL062222>
- Kilb, D., Ellis, M., Gomberg, J., & Davis, S. (1997). On the origin of diverse aftershock mechanisms following the 1989 Loma Prieta earthquake. *Geophysical Journal International*, 128(3), 557–570. <https://doi.org/10.1111/j.1365-246X.1997.tb05318.x>
- Kilb, D., Gomberg, J., & Bodin, P. (2000). Triggering of earthquake aftershocks by dynamic stresses. *Nature*, 408(6812), 570–574. <https://doi.org/10.1038/35046046>
- King, G., & Nábělek, J. (1985). Role of fault bends in the initiation and termination of earthquake rupture. *Science*, 228(4702), 984–987. <https://doi.org/10.1126/science.228.4702.984>
- Klinger, Y. (2010). Relation between continental strike-slip earthquake segmentation and thickness of the crust. *Journal of Geophysical Research*, 115(B7), B07306. <https://doi.org/10.1029/2009JB006550>
- Klinger, Y., Xu, X., Tapponnier, P., Van der Woerd, J., Lasserre, C., & King, G. C. P. (2005). High-resolution satellite imagery mapping of the surface rupture and slip distribution of the Mw 7.8, 14 November 2001 Kokoxili earthquake, Kunlun fault, northern Tibet, China. *Bulletin of the Seismological Society of America*, 95(5), 1970–1987. <https://doi.org/10.1785/0120040233>
- Kondo, H., Awata, Y., Emre, Ö., Ahmet, D., Selim, Ö., Tokay, F., et al. (2005). Slip distribution, fault geometry, and fault segmentation of the 1944 Bolu-Gerede earthquake rupture, North Anatolian fault, Turkey. *Bulletin of the Seismological Society of America*, 95(4), 1234–1249. <https://doi.org/10.1785/0120040194>
- Lasserre, C., Peltzer, G., Crampé, F., Klinger, Y., Van der Woerd, J., & Tapponnier, P. (2005). Coseismic deformation of the 2001 Mw = 7.8 Kokoxili earthquake in Tibet, measured by synthetic aperture radar interferometry. *Journal of Geophysical Research*, 110(B12), B12408. <https://doi.org/10.1029/2004JB003500>
- Lemoine, F. G., Smith, D. E., Kunz, L., Smith, R., Pavlis, E. C., Pavlis, N. K., et al. (1997). The development of the NASA GSFC and NIMA joint Geopotential model. In J. Segawa, H. Fujimoto, & S. Okubo (Eds.), *Gravity, geoid and marine geodesy* (pp. 461–469). Springer Berlin Heidelberg. https://doi.org/10.1007/978-3-662-03482-8_62
- Leroy, S., Ellouz-Zimmermann, N., Corbeau, J., Rolandone, F., Mercier de Lépinay, B., Meyer, B., et al. (2015). Segmentation and kinematics of the North America-Caribbean plate boundary offshore Hispaniola. *Terra Nova*, 27(6), 467–478. <https://doi.org/10.1111/ter.12181>
- Lin, J., & Stein, R. S. (2004). Stress triggering in thrust and subduction earthquakes and stress interaction between the southern San Andreas and nearby thrust and strike-slip faults. *Journal of Geophysical Research*, 109(B2), B02303. <https://doi.org/10.1029/2003JB002607>
- Manaker, D. M., Calais, E., Freed, A. M., Ali, S. T., Przybylski, P., Mattioli, G., et al. (2008). Interseismic plate coupling and strain partitioning in the northeastern Caribbean. *Geophysical Journal International*, 174(3), 889–903. <https://doi.org/10.1111/j.1365-246X.2008.03819.x>
- Martin, S. S., & Hough, S. E. (2022). The 8 April 1860 Jour de Pâques earthquake sequence in southern Haiti. *Bulletin of the Seismological Society of America*, 112(5), 2468–2486. <https://doi.org/10.1785/0120220016>
- Maurer, J., Dutta, R., Vernon, A., & Vajedian, S. (2022). Complex rupture and triggered aseismic creep during the 14 August 2021 Haiti earthquake from satellite geodesy. *Geophysical Research Letters*, 49(11), e2022GL098573. <https://doi.org/10.1029/2022GL098573>
- McLaren, M. K., Hardebeck, J. L., van der Elst, N., Unruh, J. R., Bawden, G. W., & Blair, J. L. (2008). Complex faulting associated with the 22 December 2003 Mw 6.5 San Simeon, California, earthquake, aftershocks, and postseismic surface deformation. *Bulletin of the Seismological Society of America*, 98(4), 1659–1680. <https://doi.org/10.1785/0120070088>

- Meade, B. J., & Loveless, J. P. (2009). Block modeling with connected fault-network geometries and a linear elastic coupling estimator in spherical coordinates. *Bulletin of the Seismological Society of America*, 99(6), 3124–3139. <https://doi.org/10.1785/0120090088>
- Oglesby, D., Archuleta, R., & Nielsen, S. (1998). Earthquakes on dipping faults: The effects of broken symmetry. *Science*, 280(5366), 1055–1059. <https://doi.org/10.1126/science.280.5366.1055>
- Oglesby, D., Archuleta, R., & Nielsen, S. (2000). Dynamic of dip-slip faulting: Explorations in two dimensions. *Journal of Geophysical Research*, 105(B6), 1–12. <https://doi.org/10.1029/2000JB900055>
- Okuwaki, R., & Fan, W. (2022). Oblique convergence causes both thrust and strike-slip ruptures during the 2021 M 7.2 Haiti earthquake. *Geophysical Research Letters*, 49(2), e2021GL096373. <https://doi.org/10.1029/2021GL096373>
- Ozawa, T., Fujita, E., & Ueda, H. (2016). Crustal deformation associated with the 2016 Kumamoto Earthquake and its effect on the magma system of Aso volcano. *Earth Planets and Space*, 68(1), 186. <https://doi.org/10.1186/s40623-016-0563-5>
- PDNA. (2021). Post-disaster needs assessment in Haiti: Earthquake of 14 August 2021 in the Southern Peninsula.
- Perfettini, H., & Avouac, J. P. (2004). Postseismic relaxation driven by brittle creep: A possible mechanism to reconcile geodetic measurements and the decay rate of aftershocks, application to the Chi-Chi earthquake, Taiwan. *Journal of Geophysical Research*, 109(B2), B02304. <https://doi.org/10.1029/2003JB002488>
- Perfettini, H., & Avouac, J. P. (2007). Modeling afterslip and aftershocks following the 1992 Landers earthquake. *Journal of Geophysical Research*, 112(B7), B07409. <https://doi.org/10.1029/2006JB004399>
- Perfettini, H., Frank, W. B., Marsan, D., & Bouchon, M. (2018). A model of aftershock migration driven by afterslip. *Geophysical Research Letters*, 45(5), 2283–2293. <https://doi.org/10.1002/2017GL076287>
- Persson, P.-O., & Strang, G. (2004). A simple mesh generator in MATLAB. *SIAM Review*, 46(2), 329–345. <https://doi.org/10.1137/S0036144503429121>
- Possee, D., Keir, D., Harmon, N., Rychert, C., Rolandone, F., Leroy, S., et al. (2019). The tectonics and active faulting of Haiti from seismicity and tomography. *Tectonics*, 38(3), 1138–1155. <https://doi.org/10.1029/2018TC005364>
- Prentice, C. S., Mann, P., Crone, A. J., Gold, R. D., Hudnut, K. W., Briggs, R. W., et al. (2010). Seismic hazard of the Enriquillo–Plantain Garden fault in Haiti inferred from palaeoseismology. *Nature Geoscience*, 3(11), 789–793. <https://doi.org/10.1038/ngeo991>
- Radiguet, M., Cotton, F., Vergnolle, M., Campillo, M., Valette, B., Kostoglodov, V., & Cotte, N. (2010). Spatial and temporal evolution of a long term slow slip event: The 2006 Guerrero slow slip event. *Geophysical Journal International*, 184(2), 816–828. <https://doi.org/10.1111/j.1365-246X.2010.04866.x>
- Raimbault, B., Jolivet, R., Calais, E., Symithe, S. J., Fukushima, Y., & Dubernet, P. (2022). Space geodetic data and fault model for the 2021 Nippes earthquake, Haiti. *Zenodo*. <https://doi.org/10.5281/zenodo.7591249>
- Rodriguez, J., Havskov, J., Sørensen, M. B., & Santos, L. F. (2018). Seismotectonics of south-west Dominican Republic using recent data. *Journal of Seismology*, 22(4), 883–896. <https://doi.org/10.1007/s10950-018-9738-9>
- Ronald, E. W., Harding, T. P., & Seely, D. R. (1973). Basic wrench tectonics. *AAPG Bulletin*, 57(1), 74–96. <https://doi.org/10.1306/819A424A-16C5-11D7-8645000102C1865D>
- Rosen, P. A., Gurrola, E., Sacco, G. F., & Zebker, H. (2012). The InSAR scientific computing environment. In *EUSAR 2012; 9th European Conference on Synthetic Aperture Radar* (pp. 730–733).
- Saint Fleur, N., Feuillet, N., & Klinger, Y. (2019). Active tectonics along the Cul-de-Sac – Enriquillo plain and seismic hazard for Port-au-Prince, Haiti. *Tectonophysics*, 771, 228235. <https://doi.org/10.1016/j.tecto.2019.228235>
- Saint Fleur, N., Klinger, Y., & Feuillet, N. (2020). Detailed map, displacement, paleoseismology, and segmentation of the Enriquillo–Plantain Garden Fault in Haiti. *Tectonophysics*, 778, 228368. <https://doi.org/10.1016/j.tecto.2020.228368>
- Scherer, J. (1912). Great earthquakes in the island of Haiti. *Bulletin of the Seismological Society of America*, 2(3), 161–180. <https://doi.org/10.1785/BSSA0020030161>
- Segall, P., & Pollard, D. D. (1980). Mechanics of discontinuous faults. *Journal of Geophysical Research*, 85(B8), 4337–4350. <https://doi.org/10.1029/JB085iB08p04337>
- Stein, R. S. (1999). The role of stress transfer in earthquake occurrence. *Nature*, 402(6762), 605–609. <https://doi.org/10.1038/45144>
- Sudhaus, H., & Jónsson, S. (2009). Improved source modelling through combined use of InSAR and GPS under consideration of correlated data errors: Application to the June 2000 Kleifarvatn earthquake, Iceland. *Geophysical Journal International*, 176(2), 389–404. <https://doi.org/10.1111/j.1365-246X.2008.03989.x>
- Symithe, S., & Calais, E. (2016). Present-day shortening in Southern Haiti from GPS measurements and implications for seismic hazard. *Tectonophysics*, 679, 117–124. <https://doi.org/10.1016/j.tecto.2016.04.034>
- Symithe, S., Calais, E., Chabaliere, J.-B. D., Robertson, R., & Higgins, M. (2015). Current block motions and strain accumulation on active faults in the Caribbean. *Journal of Geophysical Research-Solid Earth*, 120(5), 3748–3774. <https://doi.org/10.1002/2014JB011779>
- Symithe, S., Calais, E., Haase, J. S., Freed, A. M., & Douilly, R. (2013). Coseismic slip distribution of the 2010 M 7.0 Haiti earthquake and resulting stress changes on regional faults. *Bulletin of the Seismological Society of America*, 103(4), 2326–2343. <https://doi.org/10.1785/0120120306>
- Tabrez, S., Freed, A. M., Calais, E., Manaker, D. M., & McCann, W. R. (2008). Coulomb stress evolution in Northeastern Caribbean over the past 250 years due to coseismic, postseismic and interseismic deformation. *Geophysical Journal International*, 174(3), 904–918. <https://doi.org/10.1111/j.1365-246X.2008.03634.x>
- Tarantola, A. (2005). *Inverse problem theory and methods for model parameter estimation*. SIAM.
- Thio, H. K., & Kanamori, H. (1996). Source complexity of the 1994 Northridge earthquake and its relation to aftershock mechanisms. *Bulletin of the Seismological Society of America*, 86(1B), S84–S92. <https://doi.org/10.1785/BSSA08601B05S84>
- Toda, S., Stein, R. S., Richards-Dinger, K., & Bozkurt, S. B. (2005). Forecasting the evolution of seismicity in southern California: Animations built on earthquake stress transfer. *Journal of Geophysical Research*, 110(B5), B05S16. <https://doi.org/10.1029/2004JB003415>
- Uieda, L., Tian, D., Leong, W. J., Jones, M., Schlitzer, W., Grund, M., et al. (2022). PyGMT: A Python interface for the generic mapping Tools. *Zenodo*. <https://doi.org/10.5281/zenodo.6426493>
- USGS. (2021). M 7.2 - Nippes earthquake, Haiti. Retrieved from <https://earthquake.usgs.gov/earthquakes/eventpage/us6000f65h/>
- Virtanen, P., Gommers, R., Oliphant, T. E., Haberland, M., Reddy, T., Cournapeau, D., et al. (2020). SciPy 1.0: Fundamental algorithms for scientific computing in Python. *Nature Methods*, 17(3), 261–272. <https://doi.org/10.1038/s41592-019-0686-2>
- Welstead, S. T. (1999). *Fractal and wavelet image compression technique*. SPIE Optical Engineering Press. <https://doi.org/10.1117/3.353798>
- Wesnousky, S. G. (2006). Predicting the endpoints of earthquake ruptures. *Nature*, 444(7117), 358–360. <https://doi.org/10.1038/nature05275>
- Wetzler, N., Lay, T., Brodsky, E. E., & Kanamori, H. (2018). Systematic deficiency of aftershocks in areas of high coseismic slip for large subduction zone earthquakes. *Science Advances*, 4(2), eaao3225. <https://doi.org/10.1126/sciadv.aao3225>

Yin, H. Z., Xu, X., Haase, J. S., Douilly, R., Sandwell, D. T., & Mercier de Lepinay, B. (2022). Surface deformation surrounding the 2021 Mw 7.2 Haiti earthquake illuminated by InSAR observations. *Bulletin of the Seismological Society of America*, *113*(1), 41–57. <https://doi.org/10.1785/0120220109>

Zhu, L., & Rivera, L. A. (2002). A note on the dynamic and static displacements from a point source in multilayered media. *Geophysical Journal International*, *148*(3), 619–627. <https://doi.org/10.1046/j.1365-246X.2002.01610.x>